Antarctic Science 15 (1): 13–23 (2003) © Antarctic Science Ltd Printed in the UK DOI: 10.1017/S0954102003001019

Modelling the ocean circulation beneath the Ross Ice Shelf

DAVID M. HOLLAND[1], STANLEY S. JACOBS[2] and ADRIAN JENKINS[3]

[1]*Courant Institute of Mathematical Sciences, New York University, New York, NY 10012, USA*
holland@cims.nyu.edu
[2]*Lamont-Doherty Earth Observatory of Columbia University, Palisades, New York, NY 10964, USA*
[3]*British Antarctic Survey, NERC, High Cross, Madingley Rd, Cambridge CB3 0ET, UK*

Abstract: We applied a modified version of the Miami isopycnic coordinate ocean general circulation model (MICOM) to the ocean cavity beneath the Ross Ice Shelf to investigate the circulation of ocean waters in the sub-ice shelf cavity, along with the melting and freezing regimes at the base of the ice shelf. Model passive tracers are utilized to highlight the pathways of waters entering and exiting the cavity, and output is compared with data taken in the cavity and along the ice shelf front. High Salinity Shelf Water on the western Ross Sea continental shelf flows into the cavity along the sea floor and is transformed into Ice Shelf Water upon contact with the ice shelf base. Ice Shelf Water flows out of the cavity mainly around 180º, but also further east and on the western side of McMurdo Sound, as observed. Active ventilation of the region near the ice shelf front is forced by seasonal variations in the density structure of the water column to the north, driving rapid melting. Circulation in the more isolated interior is weaker, leading to melting at deeper ice and refreezing beneath shallower ice. Net melting over the whole ice shelf base is lower than other estimates, but is likely to increase as additional forcings are added to the model.

Received 1 March 2002, accepted 9 October 2002

Key words: Antarctica, isopycnic ocean model, Ross Sea

Introduction

Numerical models are beginning to provide increasingly realistic simulations of the key processes involved in establishing Antarctica's climate, which are essential for anticipating how it might change. Among the processes that remain poorly understood, however, are the thermodynamic interactions of Southern Ocean waters with the undersides of floating ice shelves that occur along the Antarctic coastline. Here we investigate these interactions by applying a coupled ocean general circulation model and a thermodynamic ice shelf base model to the Ross Sea continental shelf, including the portion beneath the Ross Ice Shelf (RIS; Fig. 1). This part of the Ross Sea has received little modelling attention until recently, despite the fact that the 0.5 M km^2 RIS accounts for nearly one third of the total Antarctic ice shelf area, and is known to influence the circulation of the Ross Sea (Jacobs *et al.* 1979, 1985).

Background

Regional glaciology

The Antarctic ice sheet, a repository for more than ninety percent of the earth's freshwater, flows seaward under the action of gravity, mainly in fast flowing ice streams that merge at their grounding lines into floating ice shelves. The current configuration of the ice sheet is believed to be in rough balance with present-day rates of accumulation and attrition, but there is little confidence in the sign of any residual imbalance (Paterson 1994). Compilations of historical accumulation data and calculations of circumpolar moisture transport give reasonable estimates for surface mass balance (Vaughan *et al.* 1999, Bromwich *et al.* 1995). Satellite observations now permit monitoring of ice elevation, and of ice front advance and retreat (Wingham *et al.* 1998, Ferrigno *et al.* 1998). Glaciological and satellite measurements also provide important clues to ice shelf behaviour (Jenkins & Doake 1991, Jenkins *et al.* 1997, Rignot 1998). Harder to assess are the oceanic processes hidden beneath the ice shelves, one of the motivations for applying numerical models to these remote domains.

As air temperatures over most of the continental ice surface remain below freezing throughout the year, the bulk of the ice sheet is returned to the ocean by iceberg calving, and by melting beneath ice shelves. The relative importance of these two attritional processes is not accurately known (Jacobs *et al.* 1992). For the RIS, a mean advance rate of 0.9 km a^{-1} (Keys *et al.* 1998), and an ice front width and mean thickness of 775 km and 250 m respectively imply a calving rate of ~175 km^3 a^{-1} to maintain a steady state area. From glaciological and oceanographic models and measurements, the area-average basal melt rate beneath the RIS has been estimated to lie between 12 and 22 cm a^{-1}, equivalent to 60–110 km^3 a^{-1} (Shabtaie & Bentley 1987, Scheduikat & Olbers 1990, Lingle *et al.* 1991, Jacobs *et al.* 1992). With 175 km^3 a^{-1} of calving, and surface accumulation over the ice shelf and surrounding catchment basin totalling around 296 km^3 a^{-1} (Vaughan *et al.* 1999), equilibrium can only be achieved at the higher end of the estimated melt rates. However, few of the budget

https://doi.org/10.1017/S0954102003001019 Published online by Cambridge University Press

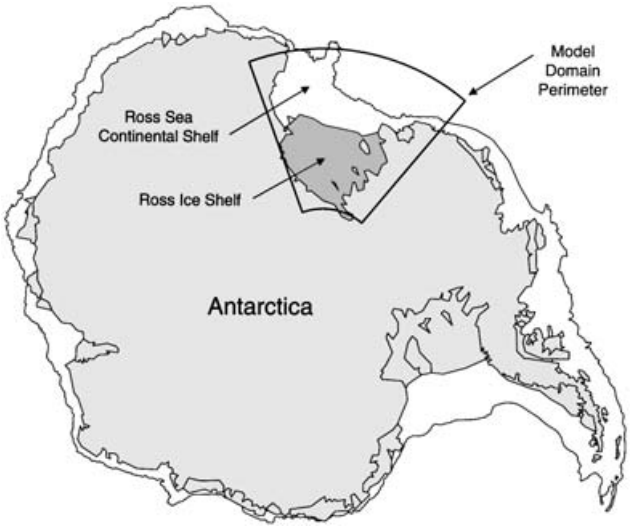


Fig. 1. Map of the Antarctic coastline and the 1000 m bathymetric contour. The model domain perimeter is shown as a sector (heavy outline) that encompasses the Ross Sea continental shelf and the Ross Ice Shelf (dark shaded).

components are well constrained, and the only direct measurement to date has demonstrated basal freezing (Zotikov *et al.* 1980). One objective of the present study has thus been to use a new numerical model to independently calculate the distribution of basal melting and freezing under the RIS, and to investigate other aspects of the sub-ice shelf circulation.

Regional oceanography

The Ross Sea continental shelf is believed to be one of the major ventilating and mixing regions for near-surface waters supplied to the deep Southern Ocean (Jacobs *et al.* 1985). Cold, fresh, near surface waters are imported from the east and north, along with tongues of warmer and saltier Modified Circumpolar Deep Water (MCDW) at intermediate depths. During winter, sea ice is generated throughout the continental shelf region, releasing brine into the underlying waters. Some of the resulting high- and low-salinity shelf waters (HSSW and LSSW) drain southward into the deeper regions beneath the RIS. There, cooling and freshening cause a net decrease in density, as parts of the ice shelf base are melted and heat is conducted into the ice (Jacobs *et al.* 1985, Nøst & Foldvik 1994, Hellmer & Jacobs 1995). After these processes have removed the available sensible heat, freezing occurs at the ice shelf base (Zotikov *et al.* 1980), and probably also within the water column (Foldvik & Kvinge 1974, Lewis & Perkin 1986). Water in contact with the ice at depth can be cooled below the sea surface freezing temperature because the *in situ* freezing point of ice in seawater decreases with increasing salinity and pressure, the latter by ~0.75°C km^{-1} (Fujino *et al.* 1974). By these processes HSSW can be transformed into Ice Shelf Water (ISW), defined as being colder than the sea surface freezing point, which is sufficiently dense to contribute to bottom water formation near the continental shelf break (Jacobs *et al.* 1985). From temperature, salinity, and current measurements along the RIS front, Jacobs *et al.* (1992) estimated a northward ISW flux of 1.4 Sv (1 Sverdrup = 10^6 m^3 s^{-1}). Based on summer thermohaline data and several year-long velocity measurements, that calculation did not account for seasonal and longer-term property changes, or transports east of 180° (Hellmer & Jacobs 1995). Circulation of warmer water beneath ice shelves can lead to much higher melt rates and shallower outflows that cannot be identified by the very cold temperatures characteristic of ISW (Potter & Paren 1985, Jenkins *et al.* 1997). Some MCDW does reach the RIS cavity, but it does not give up all its sensible heat for melting (Jacobs *et al.* 1985, 1992).

Direct measurements of water properties and currents are scarce beneath ice shelves, although valuable inferences can be drawn from ice cores and access holes (Morgan 1972, Jacobs *et al.* 1979, Zotikov *et al.* 1980, Nicholls *et al.* 1997). Ocean measurements near ice fronts can help to constrain circulation and mass balance estimates within sub-ice shelf cavities, but tend to be concentrated in the ice-free summer months (Jacobs *et al.* 1979, Pillsbury & Jacobs 1985, Potter & Paren 1985, Gammelsrød *et al.* 1994, Wong *et al.* 1998, Hellmer *et al.* 1998). Chemical tracers have been used to calculate melt water content, seawater residence time beneath ice shelves, and the characteristics of melting ice (Weiss *et al.* 1979, Michel *et al.* 1979, Jacobs *et al.* 1985, Potter & Paren 1985, Schlosser *et al.* 1990, Trumbore *et al.* 1991, Hellmer *et al.* 1998). The dynamic ranges of these tracers can be small, however, and repeated measurements are needed to assess spatial and temporal variability.

Observations such as these have demonstrated the utility of a variety of physical and chemical methods for mass balance estimates, but also that substantial differences still remain between the various estimates. Detailed sampling beneath an ice shelf is difficult and expensive, but this environment is ideal for the application of numerical models, assuming that the cavity shape, hydrodynamics and forcing can be adequately represented. In that case, the ocean density and velocity fields, ISW production and in-cavity residence times can be determined, along with net ice-ocean interactions. Model results can then be compared with independent measurements of transport and seawater properties, and the models then used to assess potential impacts of climate change.

Related modelling

A review of the status of numerical modelling of sub-ice shelf circulation and exchange with the open ocean (Williams *et al.* 1998a) highlighted the strong dependence on cavity shape, with greater melting beneath thicker ice

https://doi.org/10.1017/S0954102003001019 Published online by Cambridge University Press

and freezing beneath the thinner parts. To date, three-dimensional studies that include portions of the adjacent open ocean have largely applied sigma-coordinate models to the Filchner–Ronne and Amery ice shelf cavities (Grosfeld *et al.* 1997, Williams *et al.* 1998b, Beckmann *et al.* 1999, Gerdes *et al.* 1999). These models require many grid points to resolve baroclinic structures, and can experience pressure gradient errors near steep topography (Mellor *et al.* 1994), along with artificial diapycnal transport and tracer diffusion (Bleck 1998). A common finding of the sigma-coordinate models has been that exchange between the cavity and the open ocean is rather weak compared with the vigorous circulation that may be set up on either side of the barrier formed by the ice front. This could imply that the ice shelves are less sensitive to changes in ocean temperature and circulation than was implied by earlier one- and two-dimensional models (Williams *et al.* 1998a), and that they could potentially represent an important buffer against rapid climate change.

In search of an alternate modelling framework, we investigate the use of a common isopycnic model, which is appropriate for well stratified, deep ocean environments. The deep ocean assumption is well satisfied in the Ross Sea, which has an average depth of ~500 m. Moreover, hydrographical observations show MCDW and ISW extending over hundreds of kilometres across the continental shelf, providing evidence for significant year-round stratification in the Ross Sea. At polar latitudes, deep vertical convection can homogenize the water column. However, it is believed to be limited in both space and time (Jacobs *et al.* 1979, 1985). Unfortunately, since the existing hydrographical data is taken largely from summer hydrographical cruises, an assessment of the validity and robustness of our assumptions must await the availability of adequate winter cruise data. The isopycnic model utilized here has, nonetheless, been applied to the continental shelf region of the southern Weddell Sea, convincingly depicting circulation in the Filchner–Ronne Ice Shelf cavity (Jenkins & Holland 2002).

All ocean modelling frameworks have strengths and weaknesses. One auxiliary purpose of the present study is to model the sub-ice shelf cavity using the isopycnic framework so that a diversity of ocean modelling frameworks is applied to this important oceanographic problem. Isopycnic models switch the role of density and depth as dependent and independent variables (Bleck 1998). This approach approximates the behaviour of the real ocean, where advection and diffusion occur more readily along rather than across isopycnic (i.e. neutral) surfaces (Ledwell *et al.* 1993, Polzin *et al.* 1997). In addition, the isopycnic framework can handle flows with arbitrarily steep topography, and its grid points respond to frontal processes between adjacent water masses by migrating into regions of strong density contrast, providing resolution where and when it is most needed during a simulation

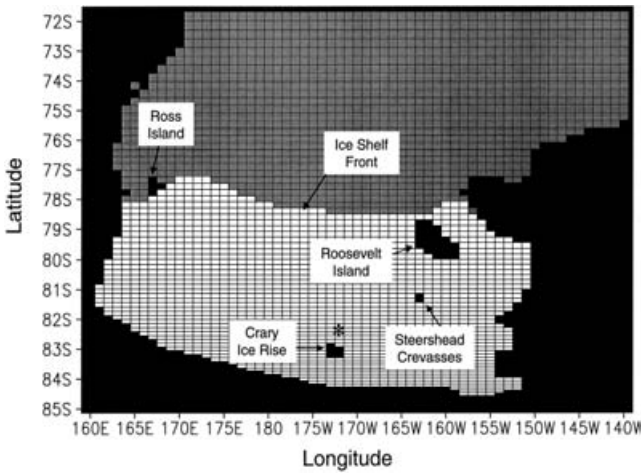


Fig. 2. Model grid cells, with land masked in solid black. The grey shaded grid cells represent the open-ocean part of the domain and the unshaded the sub-ice shelf. The ice shelf front is represented by the most northerly grid points of the sub-ice shelf domain. Lateral grid dimensions range from > 34 km to < 12 km from north to south in the full domain, with more than 1500 cells from > 24 km to < 12 km beneath the RIS. The approximate location of the J-9 drill site is indicated by the *. Land areas (in solid black) include, from east to west, Roosevelt Island, Steershead Crevasses, Crary Ice Rise, and Ross Island.

Model description

As part of a longer-term climate modelling development strategy which has as its main objective the investigation of various aspects of the climate of the polar regions, a new coupled numerical model is being constructed named the POLAIR (Polar Ocean Land Atmosphere and Ice Regional) modelling system. For the ocean component of this system we modified the Miami Isopycnic Coordinate Ocean Model (MICOM, Bleck 1998) so as to incorporate an arbitrary surface topography, i.e. an ice shelf base (Holland & Jenkins 2001). Here that ocean model is applied in a domain that includes the waters beneath the RIS and those occupying a portion of the adjacent open ocean (Fig. 1). In the modelling system, the sub-ice shelf region is isolated from the atmosphere, but influenced by the pressure of the floating ice, and by phase changes that occur at the ice shelf base. Heat and freshwater fluxes at the ice-seawater interface are parameterized with a viscous sub-layer model (Holland & Jenkins 1999). This parameterization directly accounts for the effect of congelation ice but not that of frazil ice.

The model grid (Fig. 2) is a Mercator projection such that all grid boxes are locally square, i.e. they become smaller in proportion to the cosine of the latitude as one moves southward in the domain. An average grid box side dimension in the middle of the RIS cavity is 18 km. The domain spans 63 grid points in longitude from 160°E to 140°W, and 78 in latitude from 72°S to 85°S.

https://doi.org/10.1017/S0954102003001019 Published online by Cambridge University Press

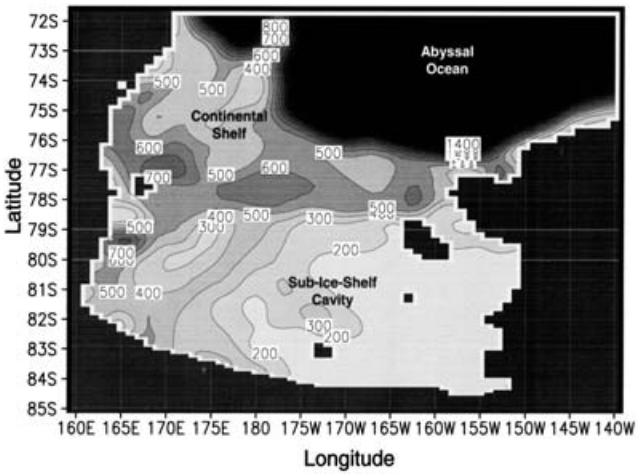


Fig. 3. Water column thickness (m) throughout the model domain, given as the difference between sea-floor depth and the sea surface or ice shelf draft. The domain can be considered to consist of three sub regions, namely, the abyssal ocean, the continental shelf, and the sub-ice shelf cavity. The dominant water column features are the jumps in thickness occurring between adjacent sub regions, that is, along the ice shelf front (particularly to the east) and along the continental shelf break.

To define the surface of the sub-ice shelf cavity, a dataset derived from the Ross Ice Shelf Geophysical and Glaciological Survey (Bentley & Jezek 1981) was used. That data is supplemented by ice front positions extracted from the Antarctic Digital Database (SCAR 1993) and height measurements taken from the USCGC *Polar Sea* in 1994 (Keys *et al.* 1998). Ice elevations are converted to ice thickness assuming hydrostatic equilibrium and including an empirical correction for trapped air in the upper part of the ice (Coslett *et al.* 1975). For the sea floor a gridded version of the RIGGS sea floor data south of 78°S (Greischar *et al.* 1981) was merged with the near global coverage ETOPO5 data base to the north (NGDC 1988). As the focus here is on the sub-ice shelf cavity, we limit the maximum open ocean depth to 1500 m. The model RIS topography and that of the underlying sea floor are based on data obtained at lower resolution than the model grid, and some data were smoothed to eliminate apparent spikes. Resulting anomalies in the basal melting and ocean circulation patterns may become apparent during future implementation of higher resolution morphologies. The model domain water column thickness resulting from the various topographical data sets is shown in Fig. 3.

To initialize the density structure of the model ocean, we use the Hydrographic Atlas of the Southern Ocean (Olbers *et al.* 1992), with an extrapolation scheme that fills the sub-ice cavity with waters similar to those at the ice shelf front. Simulations showed that temperature and salinity stabilized within a few years. Since the model vertical coordinate is isopycnic, the assignment of density coordinates to the layers is an important aspect of setting up a simulation. In

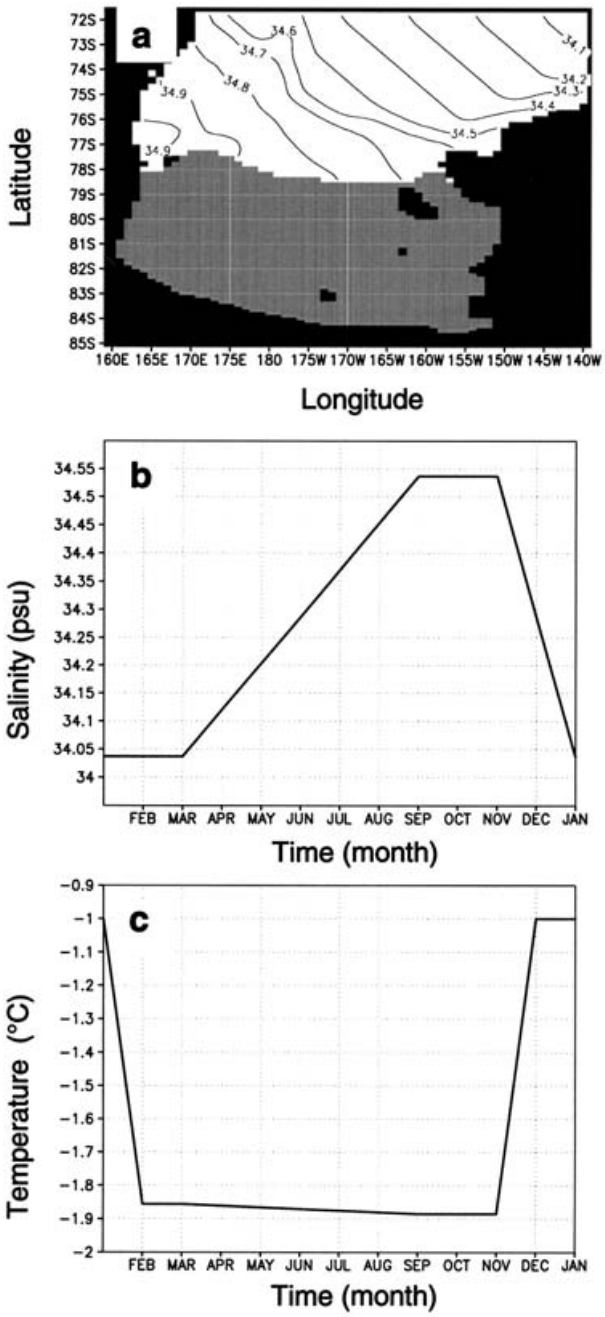


Fig. 4. a. Spatial pattern of imposed sea surface salinity field (psu) for September. The solid black shading represents the land part of the domain and the gray the ice shelf part. The imposed salinity forcing occurs only over the open ocean part of the domain and ranges from 34.1 to 34.9 (psu). **b.** Annual cycle of the mean imposed sea surface salinity field (psu). **c.** Annual cycle of the mean imposed sea surface temperature field (°C). The mean quantities in b. and c. are computed for the open-ocean part of the domain.

the real ocean mixed layer, the lightest water mass encountered in this region occurs north of the ice shelf, where summer temperatures can exceed 0.0°C and salinities can drop below 33.5 psu; the heaviest occurs in winter as

https://doi.org/10.1017/S0954102003001019 Published online by Cambridge University Press

HSSW, with properties near -1.9°C and 34.9 psu. In the ocean interior, well below the mixed layer, the thermohaline field can be well represented in density-coordinate space by a constant temperature of -1.9°C and a salinity range of 34.4 to 34.9 psu. Linearly dividing these interior ocean density extremes into ten equal intervals encompasses the density range observed in the cavity (Jacobs *et al.* 1979).

Sponge zones three grid cells wide are used to restore temperature, salinity, and layer thickness along the northern and eastern sidewalls of the open ocean part of the domain. These zones are designed to provide reasonable ocean boundary conditions and to prevent artificial drift due to the truncated domain. For baroclinic fields, the interior-most sponge cells are restored on a 30 day time scale while the exterior-most cells use a faster 10 day scale. For barotropic fields, the interior-most cells are restored on a five day time scale while the exterior-most cells are restored on a faster one day scale. This scheme ensures that properties at the boundary can be kept close to observed values without generating excessive gradients in the interior of the domain.

The modelling system does not yet incorporate winds or sea ice, but its sub-ice shelf region can reasonably be forced by a seasonally variable thermohaline field over the open ocean part of the domain. Since there are no year-round observations of sea surface salinity and temperature, we create a winter sea surface salinity patterned on the summer observations and peaking at 34.9 psu in the polynyas near Ross Island and along the western coastline near Terra Nova Bay (Fig. 4a). A seasonal cycle approximating the annual sea ice extent is generated by linearly ramping to and from an 0.5 psu lower summer surface salinity (Fig. 4b). Surface temperature is restored to the salinity dependent surface freezing point from February through October, and linearly ramped to and from an area-average summer surface temperature maximum of -1°C in December (Fig. 4c). A restoring time scale of 30 days for surface salinity and temperature north of the cavity, similar to the baroclinic restoring for the open ocean side walls, is a compromise between overly restoring on a daily time scale, and nudging sufficiently to follow the imposed surface hydrography on a seasonal basis.

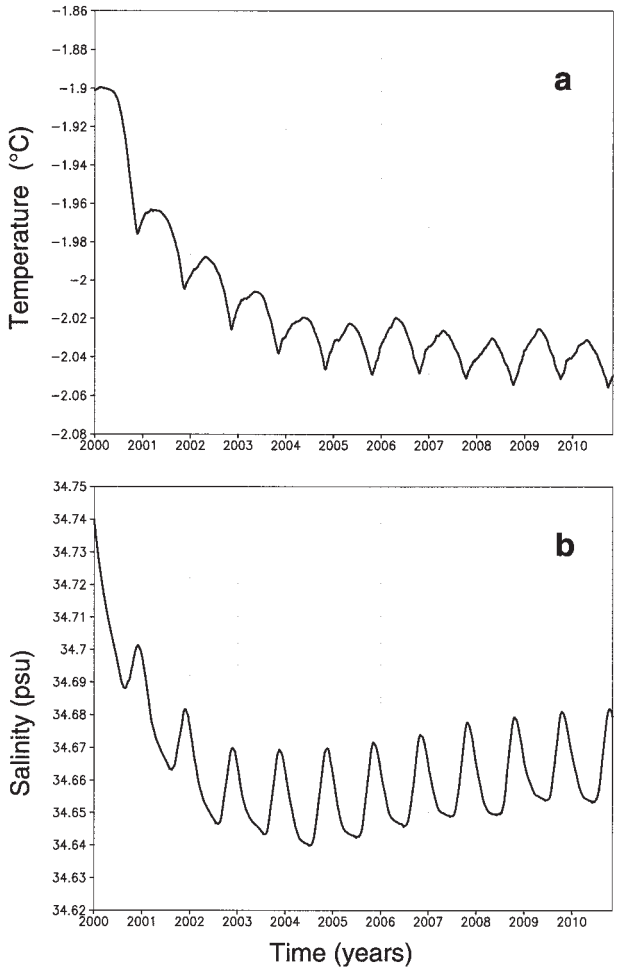


Fig. 5. Time series of cavity-integrated, layer-volume weighted, potential temperature (C) and salinity (psu) over the eleven-year model simulation period. The model integration is started nominally at year 2000.

Model simulations

Time series of modelled mean temperature (Fig. 5a) and salinity (Fig. 5b) within the cavity demonstrate that near equilibrium conditions are attained within the first several years of the model run, similar to the decadal time scale found for adjustment of geostrophic velocity and density fields for other polar ocean domains (Holland *et al.* 1996).

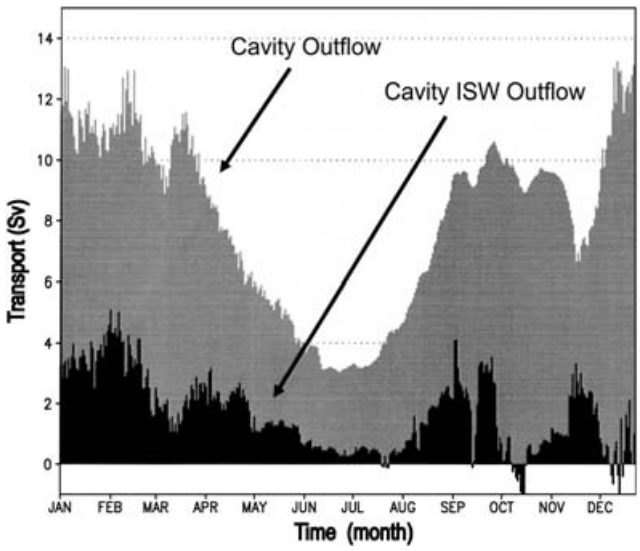


Fig. 6. Time series for the final year of the model run of total volume exchange (Sv) between the cavity and the adjacent continental shelf (grey shading). Also shown is the net outflow of ISW (black shading).

https://doi.org/10.1017/S0954102003001019 Published online by Cambridge University Press

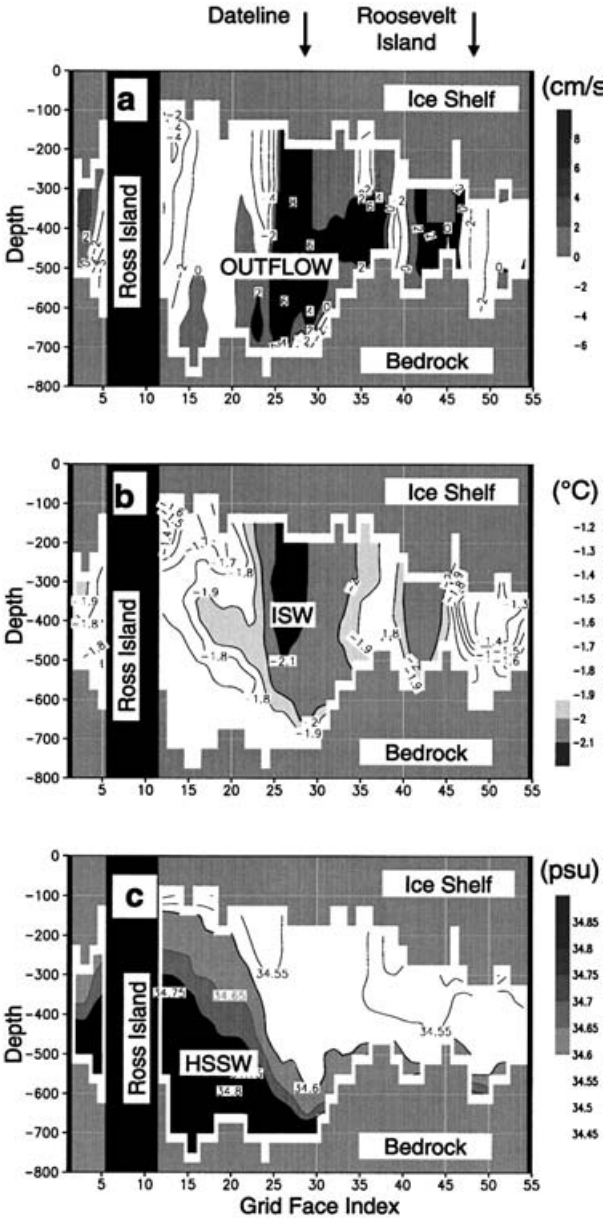


Fig. 7. Model properties along the model ice shelf front. The perspective is from within the cavity and looking northward, Ross Island is to the left (west). The vertical coordinate is depth (m); the horizontal coordinate is 'Grid Face Index'. A grid cell along the ice shelf front may have as many as three grid face indices, depending on how a grid cell protrudes into the open ocean domain. Each grid face that separates open ocean from sub-ice cavity (or island) is numbered and the index increases from left (west) to right (east). Approximately 20% of the cross-frontal flow occurs through grid faces that are outward pointing east or west. Index 28 coincides with the position of the International Dateline (180°) and indices 47 and 48 occur immediately to the north of Roosevelt Island. **a.** Outward normal velocity (cm s^{-1}) shown with shading and inward without shading. **b.** Potential temperature (°C) with waters below -1.9°C shown with shading. **c.** Salinity (psu) with waters above 34.6 psu shown with shading. All results are from April of the final year of the simulation.

Thermohaline properties change rapidly during the first three years as the initially warm cavity adjusts by excess melting. After the full integration period, the cavity temperature and salinity fluctuate around -2.04°C and 34.67 psu, with an annual cycle reflecting the surface forcing applied north of the ice shelf. A mean temperature of -2.04°C in the cavity during the final year of integration, colder than the surface freezing point of even the saltiest waters formed in the open ocean, is mainly due to net melting at the base of the ice shelf. Similarly, a mean salinity of 34.67 over the final year is less than that of the principal source waters feeding the cavity, also showing the meltwater influence. The transformation of cold, salty (denser) waters into colder but fresher (lighter) waters is consistent with observations at specific locations beneath the large ice shelves (Jacobs *et al.* 1979, Nicholls & Makinson 1998). For example, mean temperature and salinity were -2.01°C and 34.62 on a vertical profile under the RIS in December, 1978 at J9 (82.35ºS, 168.69ºW).

It may be noted that mean temperatures and salinities in the ice shelf cavity are roughly out of phase over a seasonal cycle, with temperature falling as salinity rises, and vice versa (Fig. 5). This is an indicator that, in the model at least, inflow of HSSW does dominate the average properties of the entire cavity. Exchange with the open ocean is stronger during the summer months (Fig. 6) when the average temperature of the cavity rises and the average salinity falls. This signature reflects the mixture of LSSW, MCDW and some surface water that enters the cavity along with HSSW during this period. Although the less dense water masses do not penetrate far into the cavity, a large proportion of the cavity volume lies close to the ice front where seasonal variations are strong. (Note the exaggerated area to the south in the Mercator diagram of Fig. 3, compared with the more accurate areal representation of Fig. 1.)

Ice shelf front

Vertical transects following the front of the ice shelf (Fig. 7) allow a rough evaluation of properties and transports near a section where oceanographic measurements have been made. The comparison will not be exact as the ocean stations were occupied from ships positioned within a few kilometres north of the ice while the model transect runs through the northernmost line of grid cells within the cavity. In addition, north–south gradients can be strong in this region. Nonetheless, there are several qualitative similarities along with differences that suggest improvements needed in the model ocean circulation.

The dominant pattern in Fig. 7a is one of vertical homogeneity and a series of alternating bands of northward and southward flow, with maximum velocities < 10 cm s^{-1}. A similar pattern of vertical coherence has emerged from moored current meters and geostrophic analysis of thermohaline data along the ice front (Pillsbury & Jacobs

https://doi.org/10.1017/S0954102003001019 Published online by Cambridge University Press

1985, Locarnini 1994). On the left in the figure, flow into McMurdo Sound on the eastern side, and out from beneath the ice shelf on the western side is consistent with observations (Lewis & Perkin 1985). Similarly, persistent northward flow has been measured and modelled in ISW near the dateline, here the largest region of outflow, near 'Grid Face Index' 25–30. While there are a greater number of alternating northward and southward flow bands than suggested by prior analyses (Locarnini 1994, Rock *et al.* 1994), the overall temperature and salinity fields (Fig. 7b & c) approximate summer observations reported by Jacobs & Giulivi (1998). HSSW occupies the western sector, with a shallow dome near Ross Island, where the higher salinities correspond to inflows and lower salinities to outflows. However, the persistent outflow observed east of Roosevelt Island is here replaced by inflow of MCDW, a water mass that is commonly observed to enter the cavity above a submarine rise west of the Island (Hellmer & Jacobs 1995).

The volume outflow across the ice front climbs from a minimum below 4 Sv in June to maxima above 12 Sv in December and January, with an annual mean of 8.1 (Fig. 6). The annual mean ISW volume outflow is 1.6 Sv, although there is much variability, including short periods when recirculation of ISW back into the cavity dominates to give a net inflow. ISW transport follows a different pattern than the total volume transport, particularly during spring, and its strong seasonal variability may have implications for interpreting the predominantly summer observations. For example, an estimated transport of 1.4 Sv for the primary ISW outflow region (Jacobs *et al.* 1992) was based in part on a temperature field measured during a period when the model shows the highest outflow. It should be noted that ISW is defined here to include all seawater with a temperature below -1.9°C, and that meltwater makes up only a small fraction of the modelled ISW outflow.

Layer properties

Insight into cavity dynamics can be gained by looking at properties of the top (mixed) layer and a near-bottom layer. The mixed layer flow field beneath the ice shelf (Fig. 8a & b) is mainly toward the north and west and is more sluggish than over the open ocean where surface restoring occurs. The near-bottom layer beneath the ice shelf (Fig. 8c & d) has a net south-east flow. Water of this density class only contains mass in the southern and western parts of the cavity.

As an aid to tracking water mass pathways and transformations, two artificial tracers were implemented. An ideal age tracer allows a water mass to age relative to the start time of the model simulation, with any water in contact with the open ocean surface having its age reset to zero. Most of the near-bottom isopycnic layer (Fig. 8c) shows an age of 0–6 years within the cavity. A pool of water to the north of Crary Ice Rise contains 11 year old water in a local depression (Fig. 3) that is relatively isolated from its surroundings. Relatively young HSSW enters the cavity at depth from the western continental shelf, travelling south and east along the grounding line. The transformation into mixed layer waters in the far south and east is slow, as is the subsequent north-west flow back toward the cavity opening. In the north-west HSSW takes a much shorter circuit into the cavity in the west and back out near the dateline. Real ocean CFC concentrations in water which has circulated beneath and has been modified by the RIS indicate that the transformation time from HSSW to ISW can be as short as 3.5 years (Trumbore *et al.* 1991).

A glacial meltwater fraction tracer indicates the proportion of water that has been added from the ice shelf base (Fig. 8a). Its concentration increases during melting, but is unaffected by freezing, the assumption being that the melt, once formed, will be evenly distributed throughout the mixed layer. This behaviour more closely resembles that of tracers such as oxygen-18 and helium, where the impact of freezing is small, than that of salinity, where the effects of melting and freezing are almost equal and opposite. In the mixed layer, the meltwater fraction reaches a maximum in the south-eastern corner of the cavity, where upwelling of HSSW fuels melting of the thickest ice, but the sluggish flow removes the melt rather slowly. In contrast, water that is flushed in and out of the cavity by the more vigorous circulation in the northwest acquires a relatively small concentration of melt.

The circulation in these two layers highlights the weak thermohaline circulation within the interior of the cavity and the much more active flushing of the near ice front regions, particularly those in the west.

Ice shelf base

The heat and freshwater fluxes at the base of the ice shelf are parameterized according to the viscous sub-layer model. A time series during the final year of the integration (Fig. 9) shows the variability of melting and freezing, with respective means of +9.2 and -1.0 cm a^{-1}. The seasonality displays a peak in the net melt rate of ~14 cm a^{-1} at the end of winter, and the annual average is a net melt rate of +8.2 cm a^{-1}. Freezing is an order of magnitude less than melting, and appears to rise as melting declines. The timing of the peak in melting indicates that the winter inflow of HSSW is responsible and confirms that the greater exchange across the ice front during the summer months (Fig. 6) does not carry waters far into the cavity.

The spatial pattern of melting delineates the major melting and freezing zones (Fig. 10). The most intense melting occurs near the ice front, particularly in the west, where the greatest seasonality is also seen, associated with the movement of open ocean waters near the front. Interior zones of persistent melt occur where the ice draft is deep, particularly along the grounding line. The main freezing

https://doi.org/10.1017/S0954102003001019 Published online by Cambridge University Press

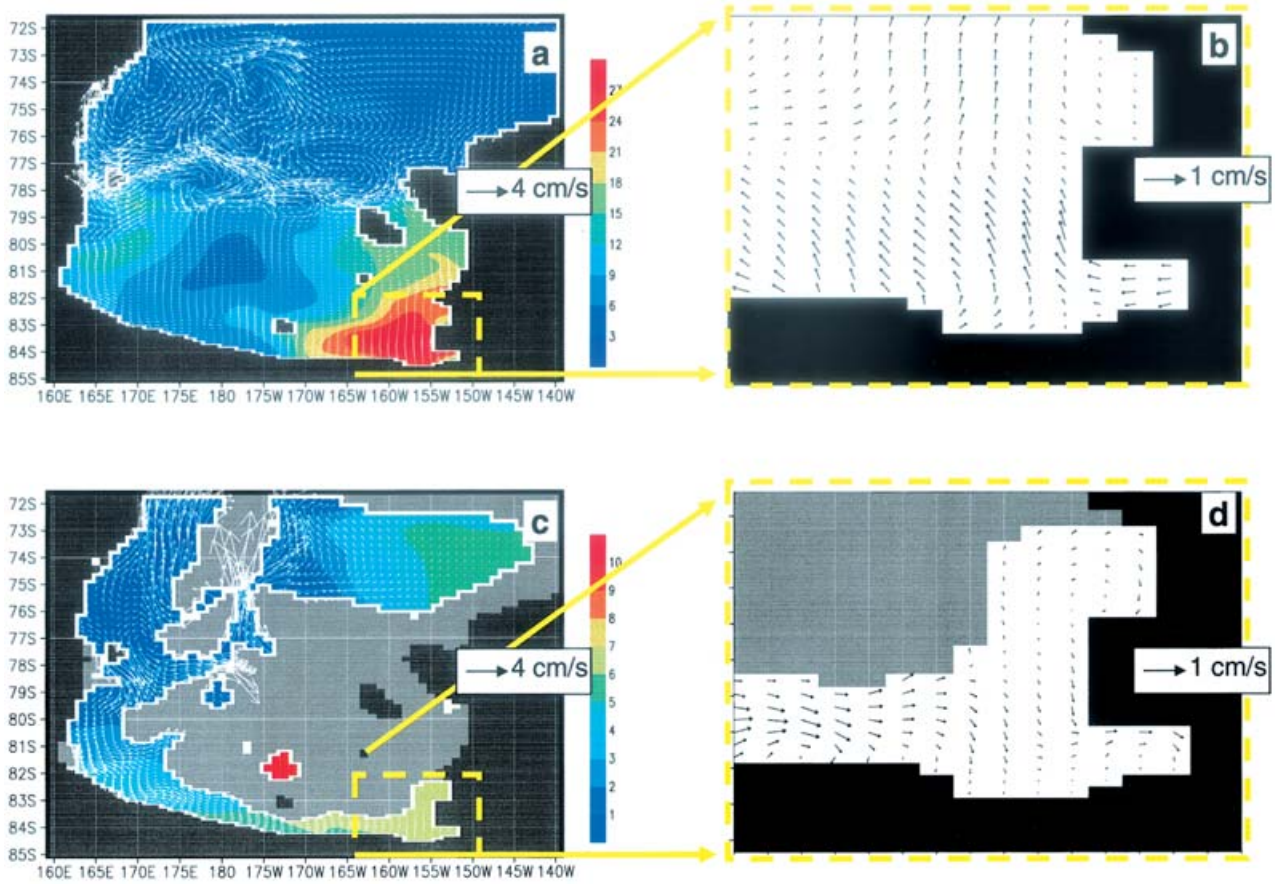


Fig. 8. a. The mixed-layer flow field (cm s^{-1}) is shown overlaying a glacial meltwater fraction tracer (units in ppt, scale is color bar to right). **b.** A zoom-view of the flow field (cm s^{-1}) in the south-eastern portion of the cavity. **c.** The flow in an interior isopycnic layer (σ_θ=28.07 $kg.m^3$, layer 10) is shown overlaying an ideal age tracer (age in years, scale is colour bar to right). **d.** A zoom-view of the flow field (cm s^{-1}) in the south-eastern portion of the cavity. The black shading represents land areas and the grey represents area where an ocean layer is massless. All results represent an average over April of the final year of the model run.

zone, and hence the likely accumulation region of marine ice (i.e. ice that forms *in situ* at the base of the ice shelf), is in the central region, aligned with the primary ISW outflow pathway. Most of the basal area is relatively quiescent, i.e. with rates < ± 2.0 cm a^{-1}, indicating that an 'ice-pump' (Lewis & Perkin 1986) appears not to be vigorous everywhere along the ice shelf base. The highest freezing rates in the interior occur near Crary Ice Rise, in a zone that includes the location of the J9 borehole.

Conclusions

Numerical modelling of the cavity beneath the RIS is a feasible means to fill gaps in our knowledge of this oceanographically extreme and geographically isolated area. At its present state of development, the modified MICOM reproduces many of the observed and expected features of the sub-ice shelf circulation. In particular, some prominent features of the observed ice front hydrography, such as the locations and properties of the main HSSW inflows and ISW outflows, are well reproduced. MCDW also reaches the model ice front, in accord with observation, but its location in the model is too far to the east. The ultimate destination of the dense shelf waters formed in the model appears to be a reasonable representation of reality. In the west, some HSSW moves northward directly off the shelf, while the portion that flows southward beneath the ice shelf emerges as ISW and leaves the shelf near the dateline (Fig. 8c).

The model melts the base of the ice shelf at an average rate lower than that of other calculations (Jacobs *et al.* 1992, Assman *et al.* 2003, Smethie personal communication 2002). The spatial distribution, with melting around the perimeter, peaking at an annual mean of 123 cm a^{-1} near the ice front and broad interior regions of gentle freezing, is in general agreement with what has been inferred from observations. The low value for the net basal melting may be an indication that the modelled thermohaline sub-ice circulation only accounts for a portion of the mass loss, and that other forcings may play a key role in enhancing the

https://doi.org/10.1017/S0954102003001019 Published online by Cambridge University Press

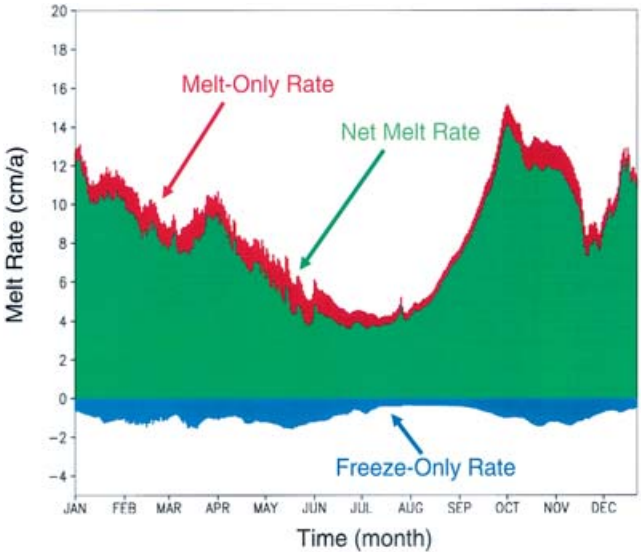


Fig. 9. Time series of the basal rates in freshwater equivalent (cm a^{-1}) of 'melt-only' (red), 'freeze-only' (blue), and 'net melt' (green) for the final year of the model run.

melt rate. We note that most estimates appear lower than needed to keep the ice shelf from thickening, i.e. to remain consistent with satellite data over the past decade.

The most striking feature of the model circulation is the contrast between the active ventilation of the near ice front region and the sluggish circulation over much of the interior. This is the result of the broad region of limited water column thickness in the south and east of the cavity, which forms an effective dead end for waters entering the region from the north and west. Density forcing generated by seasonal changes in the water column north of the ice front forces an active circulation only near the ice front, particularly in the west where the densest HSSW is formed and the cavity is most open. This feature of the circulation differentiates the sub-RIS cavity from the one beneath the Filchner–Ronne Ice Shelf, where a deep channel in the interior allows HSSW formed in the far west to circulate throughout the cavity and emerge in the east (Jenkins & Holland 2002). With a much more efficient transport of heat to the base of the thickest parts of that ice shelf, a more active 'ice-pump' results there, with higher melting and freezing rates.

This is the first three-dimensional simulation of the physical environment beneath the RIS using an isopycnic coordinate ocean model coupled with a viscous sub-layer parameterization of thermodynamic exchange at the ice shelf base. Our results, however, must be viewed as preliminary until other forcings are added and their impacts evaluated. Realistic atmospheric forcing and a sea ice model for the open ocean portion of the domain, and a tidal model for the entire region remain to be developed. Both tidal forcing (MacAyeal 1985) and the strong wind fields may impact on the vertical mixing and circulation strength, as could more detailed information on the cavity dimensions. The long-term success of this modelling activity will also hinge on the acquisition of *in situ* time series data to validate the model parameterizations of actual physical processes. Such a physically based and observationally validated model will eventually allow realistic exploration of the low frequency temporal variability of processes controlling the evolution of this system in response to climate change scenarios.

Acknowledgements

L. Greishaar provided the RIGGS data from which we

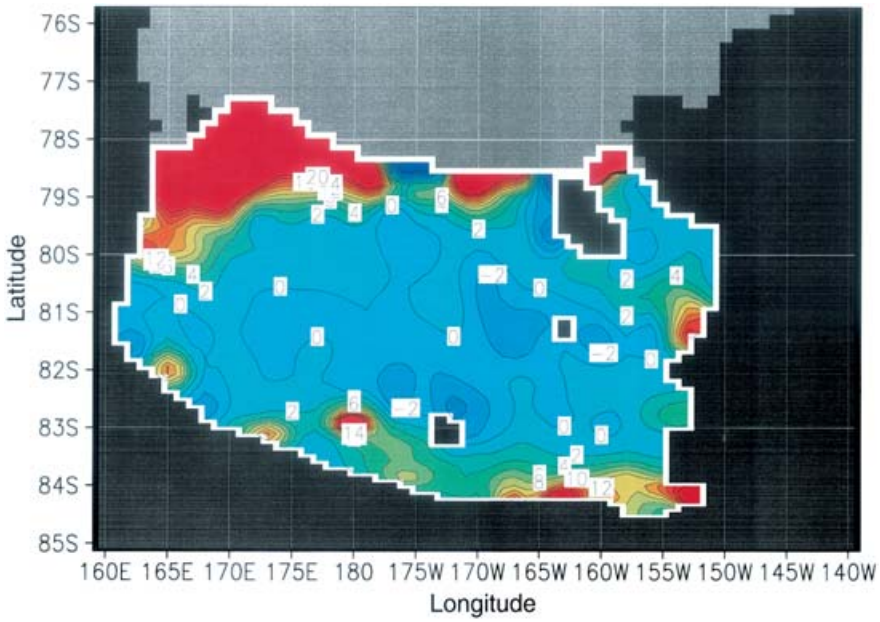


Fig. 10. Spatial pattern of melting (cm a^{-1}) over the base of the Ross Ice Shelf, averaged over the last year of the model run.

https://doi.org/10.1017/S0954102003001019 Published online by Cambridge University Press

derived ice shelf thickness. The authors gratefully acknowledge support from the Polar Research Program of the National Aeronautical Space Administration, grants NAG-5-4028 and 5-8475, and the Office of Polar Programs of the National Science Foundation, grant OPP-9984966. The Arctic Region Supercomputing Center, University of Alaska, Fairbanks, provided supercomputing time. J.-L. Tison is thanked for constructive criticism in his role as a reviewer that has led to significant improvement in the paper. The authors also thank M. van Woert for his helpful editorial comments.

References

Assmann, K., Hellmer, H.H. & Beckmann, A. 2003. Seasonal variation in circulation and water mass distribution on the Ross Sea continental shelf. *Antarctic Science*, **15**, 3–11.

Beckmann, A., Hellmer, H.H. & Timmermann, R. 1999. A numerical model of the Weddell Sea: large scale circulation and water mass distribution. *Journal of Geophysical Research - Oceans,* **104**, 23 375–23 391.

Bentley, C.R. & Jezek, K.C. 1981. RISS, RISP and RIGGS: post-IGY glaciological investigations of the Ross Ice Shelf in the US Programme. *Journal of the Royal Society of New Zealand,* **11**, 355–372.

Bleck, R. 1998. Ocean modelling in isopycnic coordinates. *In* Chassignet, E.P. & Verron, J., *eds*. *Ocean modelling and parameterization.* Dordrecht: Kluwer, 423–448.

Bromwich, D.H., Robasky, F.M., Cullather, R.I. & VanWoert, M.L. 1995. Atmospheric hydrologic-cycle over the Southern Ocean and Antarctica from operational numerical-analysis. *Monthly Weather Review,* **123**, 3518–3538.

Coslett, P.H., Guyatt, M. & Thomas, R.H. 1975. Optical levelling across an Antarctic ice shelf. *British Antarctic Survey Bulletin*, No. 40, 55–63.

Ferrigno, J.G., Williams, R.S., Rosanova, C.E., Lucchitta, B.K. & Swithinbank, C. 1998. Analysis of coastal change in Marie Byrd Land and Ellsworth Land, West Antarctica, using Landsat imagery. *Annals of Glaciology,* **27**, 33–40.

Foldvik, A., Gammelsrød, T. & Tørresen, T. 1985. Circulation and water masses on the southern Weddell Sea shelf. *Antarctic Research Series*, **43**, 5–20.

Foldvik, A. & Kvinge, T. 1974. Conditional instability of sea water at the freezing point. *Deep-Sea Research,* **21**, 169–174.

Fujino, K., Lewis, E.L. & Perkin, R.G. 1974. The freezing point of seawater at pressures up to 100 bars. *Journal of Geophysical Research - Oceans,* **79**, 1792–1797.

Gammelsrød, T., Foldvik, A., Nøst, O.A., Skagseth, Ø., Anderson, L.G., Fogelqvist, E., Olsson, K., Tanhua, T., Jones, E.P. & Østerhus, S. 1994. Distribution of water masses on the continental shelf in the southern Weddell Sea. *Geophysical Monographs*, **84**, 159–176.

Gerdes, R., Determann, J. & Grosfeld, K. 1999. Ocean circulation beneath Filchner–Ronne Ice Shelf from three-dimensional model results. *Journal of Geophysical Research - Oceans,* **104**, 15 827–15 842.

Greischar, L.L., Robertson, J.D., Bentley, C.R. & Clough, J.W. 1981. Sea-bottom topography and crustal structure below the Ross Ice Shelf, Antarctica. *In* Craddock, C., *ed*. *Antarctic geology and geophysics.* Madison, WI: University of Wisconsin Press, 1083–1090.

Grosfeld, K., Gerdes, R. & Determann, J. 1997. Thermohaline circulation and interaction between ice shelf cavities and the adjacent open ocean. *Journal of Geophysical Research - Oceans,* **102**, 15595–15610.

Hellmer, H.H. & Jacobs, S.S. 1995. Seasonal circulation under the eastern Ross Ice Shelf, Antarctica. *Journal of Geophysical Research - Oceans,* **100**, 10873–10885.

Hellmer, H.H., Jacobs, S.S. & Jenkins, A. 1998. Oceanic erosion of a floating Antarctic Glacier in the Amundsen Sea. *Antarctic Research Series*, **75**, 83–100.

Holland, D.M. & Jenkins, A. 1999. Modeling thermodynamic ice ocean interactions at the base of an ice shelf. *Journal of Physical Oceanography,* **29**, 1787–1800.

Holland, D.M. & Jenkins, A. 2001. Adaptation of an isopycnic coordinate ocean model for the study of circulation beneath ice shelves. *Monthly Weather Review,* **129**, 1905–1927.

Holland, D.M., Mysak, L.A. & Oberhuber, J.M. 1996. Simulation of the mixed-layer circulation in the Arctic Ocean. *Journal of Geophysical Research - Oceans,* **101**, 1111–1128.

Jacobs, S.S., Fairbanks, R.G. & Horibe, Y. 1985. Origin and evolution of water masses near the Antarctic continental margin: Evidence from $H_2{}^{18}O/H_2{}^{16}O$ ratios in seawater. *Antarctic Research Series*, **43**, 59–85.

Jacobs, S.S. & Giulivi, C. 1998. Interannual ocean and sea ice variability in the Ross Sea. *Antarctic Research Series,* **75**, 135–150.

Jacobs, S.S., Gordon, A.L. & Ardai Jr, J.L. 1979. Circulation and melting beneath the Ross Ice Shelf. *Science,* **203**, 439–443.

Jacobs, S.S., Hellmer, H.H., Doake, C.S.M., Jenkins, A. & Frolich, R.M. 1992. Melting of ice shelves and the mass balance of Antarctica. *Journal of Glaciology,* **38**, 375–387.

Jenkins, A. & Doake, C.S.M. 1991. Ice-ocean interaction on Ronne Ice Shelf, Antarctica. *Journal of Geophysical Research - Oceans,* **96**, 791–813.

Jenkins, A. & Holland, D.M. 2002. A model study of ocean circulation beneath Filchner–Ronne Ice Shelf, Antarctica: implications for bottom water formation, *Geophysical Research Letters*, **29**, 10.1029/2001GL014589.

Jenkins, A., Vaughan, D.G., Jacobs, S.S., Hellmer, H.H. & Keys, J.R. 1997. Glaciological and oceanographic evidence of high melt rates beneath Pine Island glacier, West Antarctica. *Journal of Glaciology,* **43**, 114–121.

Keys, H., Jacobs, S.S. & Brigham, L. 1998. Continued northward expansion of the Ross Ice Shelf. *Annals of Glaciology,* **27**, 93–98.

Ledwell, J.R., Watson, A.J. & Law, C.S. 1993. Evidence for slow mixing across the pycnocline from an open-ocean tracer release experiment. *Nature,* **364**, 701–703.

Lewis, E.L. & Perkin, R.G. 1985. The winter oceanography of McMurdo Sound, Antarctica. *Antarctic Research Series*, **43**, 145–166.

Lewis, E.L. & Perkin, R.G. 1986. Ice pumps and their rates. *Journal of Geophysical Research,* **91**, 11 756–11 762.

Lingle, C.S., Schilling, D.H., Fastook, J.L., Paterson, W.S.B. & Brown, T.J. 1991. A flow band model of the Ross Ice Shelf. Antarctica - response to CO_2-induced climatic warming. *Journal of Geophysical Research - Solid Earth and Planets,* **96**, 6849–6871.

Locarnini, R.A. 1994. *Water masses and circulation in the Ross Gyre and environs*. PhD thesis, Texas A&M University, 86 pp. [Unpublished].

MacAyeal, D.R. 1985: Tidal rectification below the Ross Ice Shelf, Antarctica *Antarctic Research Series,* **43**, 133–143.

Mellor, G.L., Ezer, T. & Oey, L.Y. 1994. The gradient conundrum of sigma co-ordinate ocean models. *Journal of Atmospheric and Oceanic Technology,* **11**, 1126–1134.

Michel, R.L., Linick, T.W. & Williams, P.M. 1979. Tritium and carbon-14 distributions in seawater from under the Ross Ice Shelf Project ice hole. *Science,* **203**, 445–446.

Morgan, V.I. 1972. Oxygen isotope evidence for bottom freezing on the Amery Ice Shelf. *Nature,* **238**, 393–394.

NGDC. 1988. *Five minute gridded world elevations and bathymetry (ETOPO5)*. National Geophysical Data Center, Boulder, Colorado. http://www.ngdc.noaa.gov/mgg/index.html

Nicholls, K.W. & Makinson, K. 1998. Ocean circulation beneath the western Ronne Ice Shelf, as derived from *in situ* measurements of water currents and properties. *Antarctic Research Series,* **75**, 301–318.

https://doi.org/10.1017/S0954102003001019 Published online by Cambridge University Press

NICHOLLS, K.W., MAKINSON, K. & JOHNSON, M.R. 1997. New oceanographic data from beneath Ronne Ice Shelf, Antarctica. *Geophysical Research Letters,* **24**, 167–170.

NØST, O.A. & FOLDVIK, A. 1994. A model of ice-shelf ocean interaction with application to the Filchner–Ronne and Ross ice shelves. *Journal of Geophysical Research - Oceans,* **99**, 14 243–14 254.

OLBERS, D.J., GOURETZKI, V., SEISS, G. & SCHRÖTER, J. 1992. *The hydrographic atlas of the Southern Ocean*. Bremerhaven: Alfred Wegener Institute. http://www.awi-bremerhaven.de/Atlas/SO

PATERSON, W.S.B. 1994. *The Physics of Glaciers.* New York: Elsevier, 480 pp.

PILLSBURY, R.D. & JACOBS, S.S. 1985. Preliminary observations from longterm current meter moorings near the Ross Ice Shelf, Antarctica. *Antarctic Research Series,* **43**, 87–107.

POLZIN, K.L., TOOLE, J.M., LEDWELL, J.R. & SCHMITT, R.W. 1997. Spatial variability of turbulent mixing in the abyssal ocean. *Science,* **276**, 93–96.

POTTER, J.R. & PAREN, J.G. 1985. Interaction between ice shelf and ocean in George VI Sound, Antarctica. *Antarctic Research Series,* **43**, 35–58.

RIGNOT, E. 1998. Fast recession of a West Antarctic Glacier. *Science,* **281**, 549–551.

ROCK, S., HELLMER, H.H. & JACOBS, S.S. 1994. Mass and heat transports beneath the Ross Ice Shelf. *EOS Transactions*, **75**, 223.

SCAR. 1993. *Antarctic Digital Database*. Cambridge: Scientific Committee on Antarctic Research. http://www.nerc-bas.ac.uk/public/magic/add.html

SCHEDUIKAT, M. & OLBERS, D.J. 1990. A one-dimensional mixed layer model beneath the Ross Ice Shelf with tidally induced vertical mixing. *Antarctic Science,* **2**, 29–42.

SCHLOSSER, P., BAYER, R., FOLDVIK, A., GAMMELSRØD, T., ROHARDT, G. & MÜNNICH, K.O. 1990. O-18 and helium as tracers of ice shelf water and water ice interaction in the Weddell Sea. *Journal of Geophysical Research - Oceans,* **95**, 3253–3263.

SHABTAIE, S. & BENTLEY, C.R. 1987. West Antarctic ice streams draining into the Ross Ice Shelf: configuration and mass balance. *Journal of Geophysical Research,* **92**, 1311–1336.

TRUMBORE, S.E., JACOBS, S.S. & SMETHIE, W.M. 1991. Chlorofluorocarbon evidence for rapid ventilation of the Ross Sea. *Deep-Sea Research,* **38**, 845–870.

VAUGHAN, D.G., BAMBER, J.L., GIOVINETTO, M., RUSSELL, J. & COOPER, A.P.R. 1999. Reassessment of net surface mass balance in Antarctica. *Journal of Climatology*, **12**, 933–946.

WEISS, R.F., OSTLUND, H.G. & CRAIG, H. 1979. Geochemical studies of the Weddell Sea. *Deep-Sea Research,* **26**, 1093–1120.

WILLIAMS, M.J.M., JENKINS, A. & DETERMANN, J. 1998a. Physical controls on the ocean circulation beneath ice shelves revealed by numerical models. *Antarctic Research Series,* **75**, 285–299.

WILLIAMS, M.J.M., WARNER, R.C. & BUDD, W.F. 1998b. The effects of ocean warming on melting and ocean circulation under the Amery Ice Shelf, East Antarctica. *Annals of Glaciology,* **27***,* 75–80.

WINGHAM, D.J., RIDOUT, A.J., SCHARROO, R., ARTHERN, R.J. & SHUM, C.K. 1998. Antarctic elevation change from 1992 to 1996. *Science,* **282**, 456–458.

WONG, A.P.S., BINDOFF, N.L. & FORBES, A. 1998. Ocean-ice shelf interaction and possible bottom water formation in Prydz Bay, Antarctica. *Antarctic Research Series,* **75**, 173–188.

ZOTIKOV, I.A., ZAGORODNOV, V.S. & RAIKOVSKY, J.V. 1980. Core drilling through the Ross Ice Shelf (Antarctica) confirmed basal freezing. *Science,* **207**, 1463–1465.

https://doi.org/10.1017/S0954102003001019 Published online by Cambridge University Press

https://doi.org/10.1017/S0954102003001019 Published online by Cambridge University Press